Vacancy release upon heating of an ultrafine grain Al-Zr alloy: In-situ observations and theoretical modeling

Williams Lefebvre, N.V. Skiba, F. Chabanais, M.Yu. Gutkin, Lorenzo Rigutti, M.Yu. Murashkin, T.S. Orlova

Version of Record: https://www.sciencedirect.com/science/article/pii/S0925838820348180
Manuscript_89428517851671611e65287ee775145d

Vacancy release upon heating of an ultrafine grain Al-Zr alloy: in-situ observations and theoretical modeling

W. Lefebvre[1], N.V. Skiba[2,3], F. Chabanais[1], M.Yu. Gutkin[2,3], L. Rigutti[1], M.Yu. Murashkin[4,5], T.S. Orlova[6]

[1]Normandie University, UNIROUEN, INSA Rouen, CNRS, Groupe de Physique des Matériaux, 76000 Rouen, France

[2]Institute for Problems in Mechanical Engineering, Russian Academy of Sciences, 199178 St. Petersburg, Russia

[3]Peter the Great St. Petersburg Polytechnic University, 195251 St. Petersburg, Russia

[4]Saint Petersburg State University, 198504 St. Petersburg, Russia

[5]Institute of Physics of Advanced Materials, Ufa State Aviation Technical University, 450000 Ufa, Russia

[6]Ioffe Institute, Russian Academy of Sciences, 194021 St. Petersburg, Russia

Keywords: cavities, pore, UFG, vacancy, grain boundary, severe plastic deformation, in-situ, annealing, disclination.

Abstract

The present study demonstrates the direct observation of pore formation by rapid release of vacancies in ultrafine grain (UFG) Al-0.4at%Zr alloy during in-situ annealing in a scanning transmission electron microscope. The ultrafine grain structure was preliminary obtained by high pressure torsion processing at a hydrostatic pressure of 6 GPa up to 10 revolutions. In-situ annealing reveals the rapid formation of pores in triple junctions (TJs) of grain boundaries (GBs) during the first few minutes followed by their subsequent slow resorption with the complete disappearance of some of them. During annealing, no noticeable displacement of GBs is observed. By considering the evolution of non-equilibrium GBs inherited by the severe plastic deformation, a theoretical description is suggested which describes: (i) the pore formation at disclinated TJs as a thermodynamically driven process of free volume dissolution through generation of vacancies, which then migrate to the TJs and coagulate at them with growth of the pores diminishing the strain energy of the TJ disclinations, and (ii) further decrease of the TJ disclination strain energy through the climb of extrinsic GB dislocations towards the disclinated TJs, accompanied with dissolution of the TJ pores by emission of vacancies which provide the dislocation climb. The rapid release of

excess vacancies during the early stage of heat treatment is consequently identified as a phenomenon responsible for accelerated atomic mobility. This work hence provides a new perspective for understanding the accelerated precipitation kinetics observed in severely deformed alloys.

1. Introduction.

Ultrafine grain (UFG) microstructure are known to lead to very high strength often combined with significant ductility [1–3]. Such a combination of properties can even be improved by means of the fine scale precipitation of a second phase [4–6]. Furthermore, faster precipitation kinetics is often observed if precipitation hardening treatments are applied to alloys processed by severe plastic deformation (SPD) [5–7]. To explain this, numerous effects and interactions between defects can be considered and their influence is potentially variable from one alloy system to the other. For example, UFG can promote solute segregation and/or heterogeneous precipitation [3,8–12], whereas the importance of such phenomena would be negligible in a coarse grain structure. In addition, SPD is known to produce large quantities of excess vacancies [13–21]. However, giving an experimental evidence of the effect of vacancies on precipitation is a very challenging task. Previously, Deschamps et al. [5] suggested that deformation induced non-equilibrium vacancies may contribute to nucleation, rapid growth and coarsening of precipitates formed along deformation induced dislocations and grain boundaries (GBs). In a paper by Wang et al. [7], who studied the precipitation in an Al-Zn-Mg-Cu alloy processed by surface abrasion, it was proposed that accelerated precipitation kinetics and selection of phases were driven by two phenomena. First, accelerated diffusivity along GBs and sub-GBs were calculated and found responsible for the accelerated precipitation and growth of phases. But to explain how solutes could be transported to these boundaries, these authors proposed that certain solute-vacancies complex could form, as observed by positron annihilation spectroscopy [20], and promote the selected transport of some solutes to the boundaries.

The purpose of the present work is to help elucidating the mechanisms at stake in the very early stages of precipitation in an alloy which has first undergone a severe plastic deformation. Instead of investigating the material at the scale of precipitation (i.e. nanometer scale), it has been chosen to follow the microstructure evolution at a larger scale, in order to reveal the behaviour and potential influence of GBs and dislocations. To this aim, it is proposed to follow in-situ, in a scanning transmission electron microscope (STEM), the

evolution of the severely deformed microstructure heated to the precipitation annealing temperature of a model alloy system. Such a protocol allows to follow the eventual motion of GBs or sub-GBs, of dislocations as well the nucleation and growth of precipitates.

In the selected model alloy (Al-0.4wt%Zr), in absence of SPD, significant precipitation hardening is typically obtained for annealing temperatures superior to 350 °C [22–25]. On the contrary, the same alloy system exhibits a drastically increased precipitation kinetics if previously submitted to severe plastic deformation [26–30]. Previous works have indeed demonstrated that in the UFG state, annealing temperature of 230 °C is sufficient to cause a precipitation to produce a dense precipitation of Al_3Zr phase [28–30]. An UFG structure has hence been obtained by means of high pressure torsion (HPT) [31,32]. Then, the alloy has been exposed to in-situ heating at 230°C in a scanning transmission electron microscope (STEM). This original procedure reveals the rapid formation of nanopores at GBs. The release of large amounts of vacancies induced by the rearrangement of near equilibrium GBs is the mechanism identified as responsible for the formation of pores. A physical model is proposed to describe both the formation and the evolution of these nanopores during in-situ annealing.

2. Material and experimental procedures

The Al-0.4Zr (wt.%) alloy with the chemical composition 99.25 Al, 0.393 Zr, 0.023 Si, 0.242 Fe, 0.018 Zn, 0.026 V, 0.05 - balance (wt.%) produced by combined casting and rolling (C-R) [33,34] was investigated. The material was supplied by UC RUSAL (Moscow, Russia). The alloy was subjected to long term annealing at 375 °C for 60 h. Then the samples in the shape of disc were processed by high pressure torsion (HPT) under a hydrostatic pressure of 6 GPa to ten revolutions at room temperature (RT) [32]. As a result of such treatment the disc-shaped samples with a diameter of 20 mm and a thickness of 1.2 mm were obtained. The true strain at a distance of 5 mm from the disc center was $\varepsilon \approx 6.6$. More details of the sample preparation are presented in [29].

Scanning Transmission Electron Microscopy (STEM) observations were performed using a JEOL ARM 200F operating at 200 kV. The probe size was set to 0.11 nm. The half convergence angle was 22.5 mrad. Thin foils for STEM were prepared using a standard twin jet polishing procedure. The electrolyte (2/3 methanol, 1/3 nitric acid) was used and cooled at -30°C. In large angle annular dark field (LAADF) mode in STEM, the collection angle was in

the range 20-80 mrad. In high angle annular dark field (HAADF) mode, the collection angle was in the range 80-180 mrad. The contrast in LAADF STEM is dominated by diffraction whereas images in HAADF STEM are dominated by Z-contrast and specimen thickness. For in-situ heating in STEM, the thin foil was placed in a Gatan heating double tilt specimen holder (model 652 with tantalum furnace). During in-situ heating, the temperature was directly set to 230 °C starting from room temperature. The 230 °C target temperature was reached after 30 s. The start of heating is the reference for the time recorded with each picture.

3. Results

3.1. Microstructure characterization

The characterization of the samples by X-ray diffraction (XRD) analysis, electron back-scatter diffraction (EBSD) and transmission electron microscopy (TEM) was performed in our preliminary studies and the results were reported in [29] and summarized in Table 1. In Table 1, the samples after aging and HPT processing before annealing are referred to as AG-HPT. The samples after subsequent annealing at 230 oC for 1 h and 3 h are referred to as AG-HPT-AN(1h) and AG-HPT-AN(3h), respectively. As seen in Table 1, annealing of AG-HPT sample at 230 °C for 1 h results in only slight increase of the average grain size d_{av}, whereas the continuation of annealing at the same temperature up to 3 h does not change d_{av}. According to the XRD data the annealing leads to 4-5 time decrease of dislocation density (Table 1) [29].

Table 1 : Microstructure parameters of Al-0.4Zr samples obtained by XRD and EBSD (data of [29]) are: d_{av} the average grain size; θ_{av} the average GB misorientation angle; $f_{\geq 15}$ the fraction of high-angle GBs with a misorientation angle $\theta \geq 15^{o}$; a the lattice parameter; D_{XRD} the average size of coherent scattering domains; $\langle \varepsilon^2 \rangle^{1/2}$ the level of microdistortions of the crystalline lattice; L_{dis} the dislocation density.

State	EBSD			XRD			
	d_{av}, nm	$f_{\geq 15}$, %	θ_{av}, ^{o}	a, Å	D_{XRD}, nm	$\langle \varepsilon^2 \rangle^{1/2}$, %	L_{dis}, m^{-2}
AG-HPT	945±17	78	34.8	4.0504± 0.00004	310±10	0.00580± 0.0001	$2.3 \cdot 10^{12}$
AG-HPT-AN(1h)	1170±19	84	35.1	4.0509± 0.00004	420±10	0.00150± 0.0001	$4.3 \cdot 10^{11}$
AG-HPT-AN(3h)	1125±18	85	35.6	4.0509± 0.00002	422±5	0.00180± 0.0001	$5.0 \cdot 10^{11}$

3.2. Experiment on annealing at 230 °C for 3 h in-situ in STEM

Annealing of the HPT-processed Al-0.4Zr alloy was performed in-situ at 230 °C in STEM for a maximum duration of 3 h. Attention has been paid to the evolution of microstructure at the grain scale. In the initial state, contrast inside grains (shown by arrows in Figure 1a) corresponds to dislocations. After heat treatment a part of this contrast disappears that most probably points to annihilation of these dislocations. This finding is in good agreement with the decrease of integrated dislocation density after such annealing (Table 1, the XRD data [15]). It is important to note that no noticeable displacement of GBs has been observed during in-situ annealing. Nevertheless, an important detail is revealed by focusing on areas highlighted by circles in Figure 1. In these areas, annealing involves a slight rearrangement of GBs orientation. Indeed, some GBs are shown to straighten and the angles between them approach 120 degrees. This is all the more obvious for the GBs in the upper circle of Figure 1b. Such an observation is the experimental evidence that some GBs are relaxing their configuration during in-situ annealing.

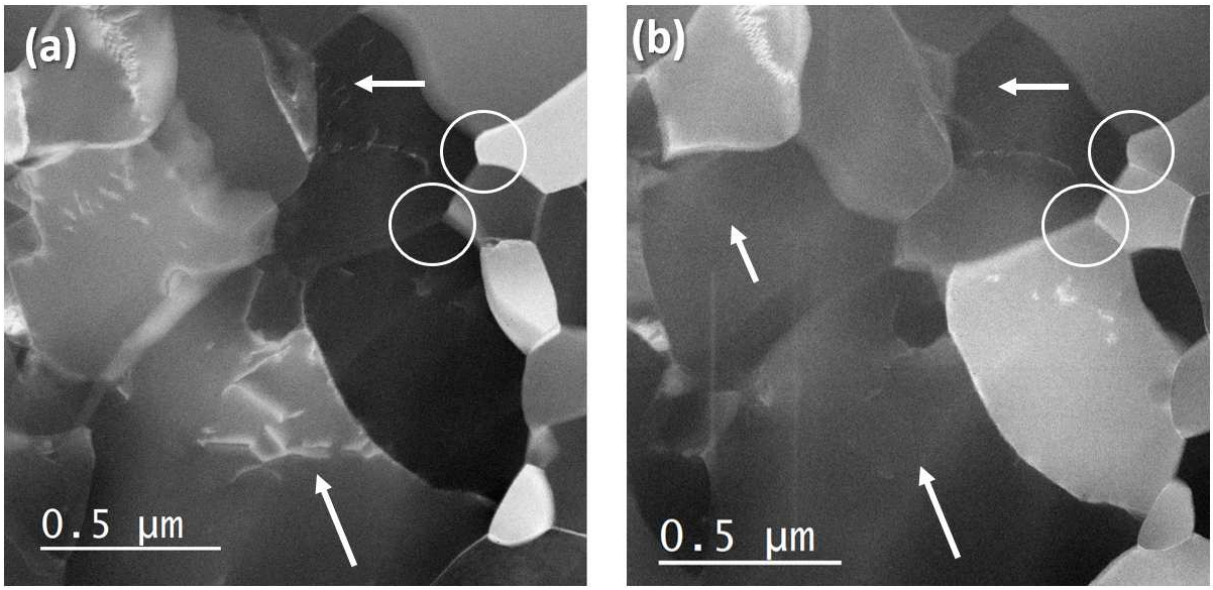

Figure 1 : LAADF STEM images of the material (a) before in-situ annealing and (b) after 8 800 s (~2h27') in-situ heating at 230 °C. Diffraction contrast allows distinguishing GBs and dislocations. In some areas pointed by arrows, dislocations are not visible after annealing. White circles outline GBs which straighten during annealing.

In Figure 2, images of the same region acquired simultaneously are displayed with two distinct contrasts. It must be pointed out that for the magnification used for images of Figure 2 and Figure 3, the formation of nanometer scale precipitates enriched in Zr cannot be followed because of their too small dimension. On the right, the contrast in LAADF is dominated by

diffraction. Hence, it is possible to distinguish grains, GBs and dislocations. On the left, a HAADF detector has been used to map the variation of specimen density. Indeed, the intensity in HAADF mode of probed volumes of identical thicknesses varies as a function of Z^n, Z being the average atomic number in the volume scanned by the probe and ranging from 1.7 to 2 [35]. In cases when no significant changes of composition are involved in the specimen, HAADF intensity varies linearly with the thickness [35]. This corresponds to the conditions of observations, for which no large Al_3Zr precipitates are present in the specimen. Further discussion of the contrast associated to pores is provided in the supplemental information, together with additional data.

Figure 2a and b display a large region of the STEM foil before the in-situ annealing. After annealing for 75 seconds, many pores are already visible in the same area (Figure 2c and d) and their location is pointed by arrows in all images for an easy comparison of associated contrasts. The formation of pores is hence found to occur at the very beginning of the in-situ heat treatment. The pores are mostly located at GB junctions. Only few of them are revealed along simple GBs. The typical size of pores is about 40-80 nm and the largest dimension does not exceed 120 nm.

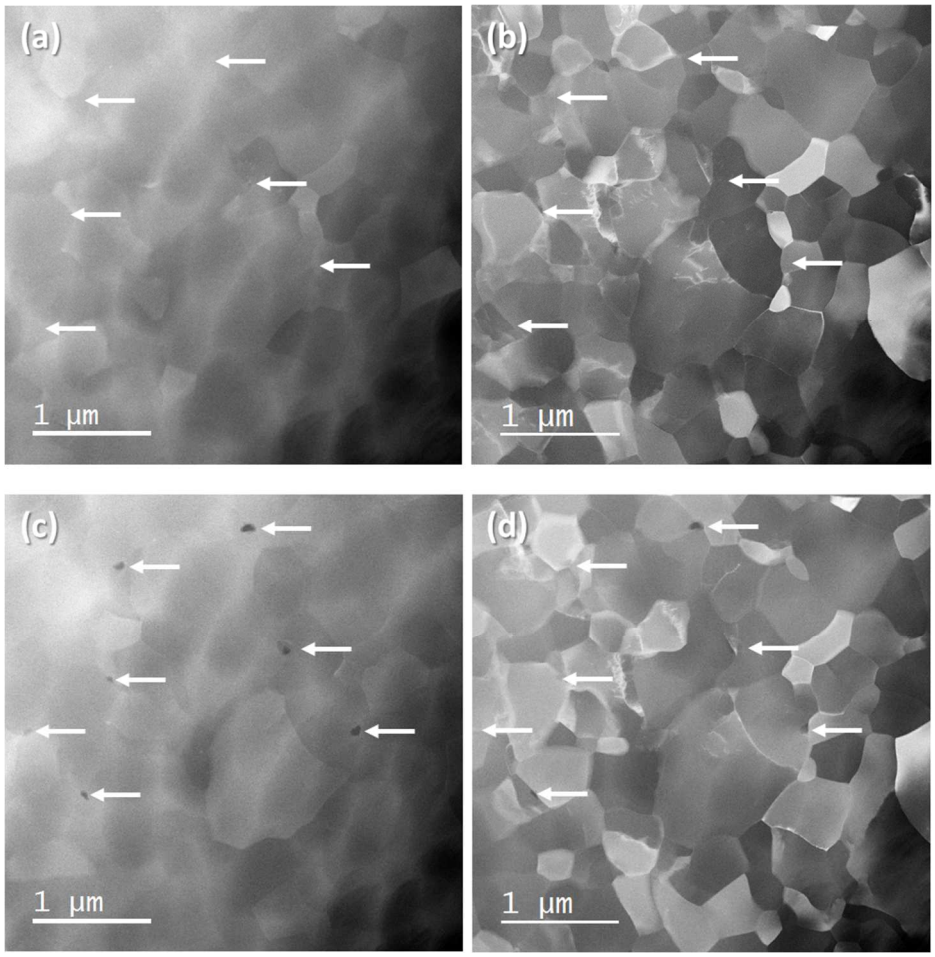

Figure 2 : STEM observations of the UFG Al-0.4wt%Zr alloy before in-situ annealing (a,b) and after 75 s of annealing at 230 °C. (a) and (c) are HAADF STEM images whereas (b) and (d) are LAADF STEM images. White arrows indicate where nanopores are forming.

After further holding at 230 °C, the size of pores decreases and some of them even disappear as seen in Figure 3(f) (see also the comment about pore's resorption in the supplemental information), which shows the same area after annealing for 8 800 s (~ 2 h 27'). A sequence of images recorded for the whole duration of the in-situ heat treatment is indeed displayed in Figure 3, where the pores are observed during an annealing time ranging from 75s to 8 800s.

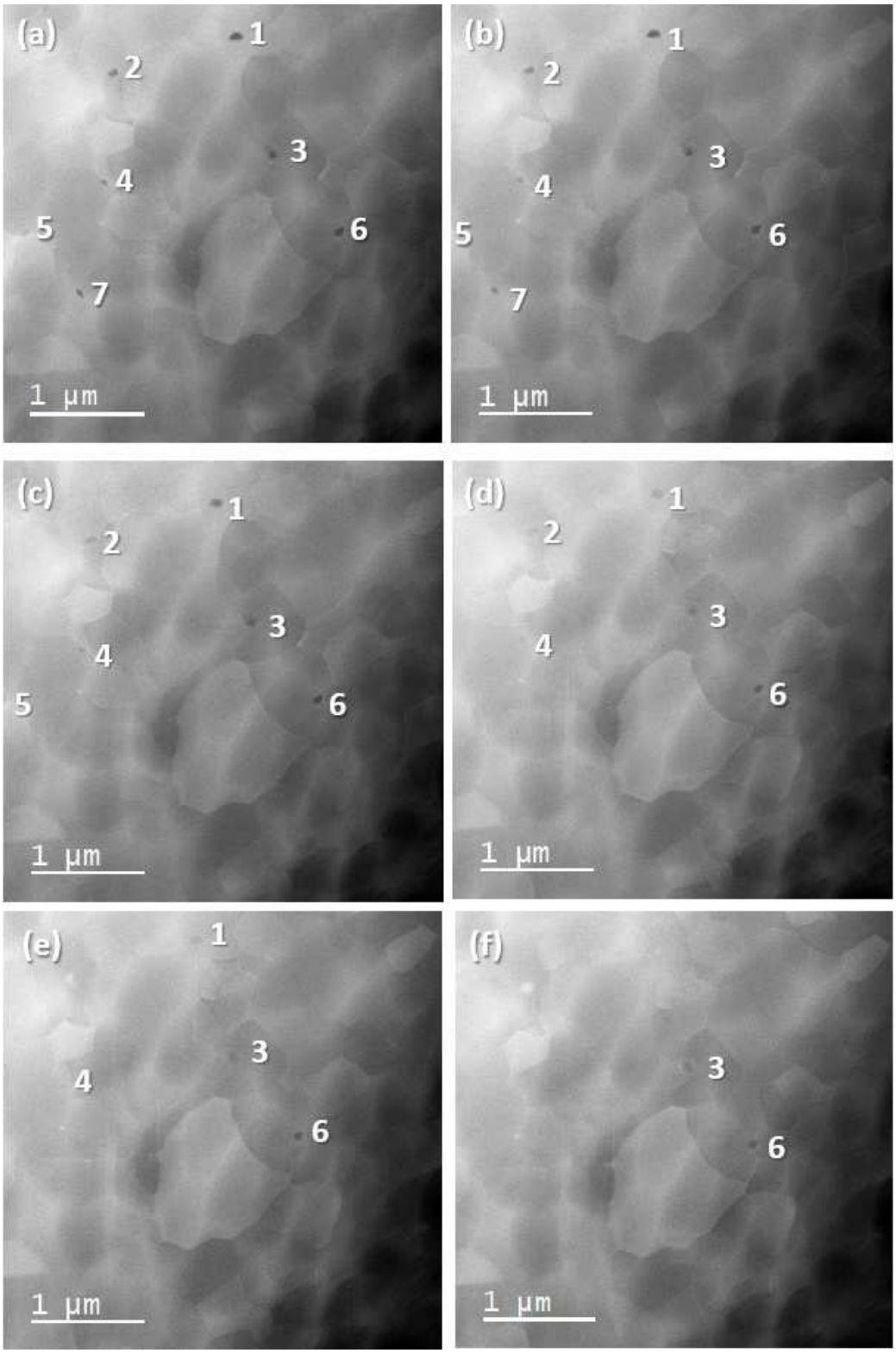

Figure 3 : HAADF STEM images of the UFG Al-0.4w%Zr alloy recorded at different times of in-situ annealing at 230 °C: (a) 75 s, (b) 500 s, (c) 950 s, (d) 2 100 s, (e) 3 640 s, (f) 8 800 s. Numbers are placed to distinguish each nanopore.

Table 2 : Metrics associated to the pores observed at the very beginning of the in-situ annealing in STEM (Figure 3a). Initial cross sections were measured on the image. An equivalent diameter was deduced from cross sections. An estimation of the volume of pores was calculated using the assumption of a spherical shape.

Pore	Initial cross section (nm^2)	Equivalent diameter (nm)	Estimated volume (nm^3)
1	(6.0 ±0.3) 10^3	87 ± 5	(3.5 ±0.3) 10^5
2	(4.2 ±0.2) 10^3	73± 5	(2.1 ±0.2) 10^5
3	(3.6 ±0.2) 10^3	68 ± 4	(1.6 ±0.2) 10^5
4	(1.7 ±0.1) 10^3	46 ± 3	(0.5 ±0.1) 10^5
5	(3.3 ±0.2) 10^3	65 ± 4	(1.5 ±0.2) 10^5
6	(4.9 ±0.3) 10^3	79 ±5	(2.6 ±0.2) 10^5
7	(3.0 ±0.2) 10^3	61 ± 4	(1.2 ±0.1) 10^5

Because of a slight shift of the specimen, pore number 5 could not be seen in all images. Attributing number to pores allows following their distinct evolution during annealing. As illustrated in Table 2, at the start of heat treatment, the diameter of pores ranges from 40 nm to 90 nm and their estimated volume is found to range from 0.5 10^5 nm^3 to 3.5 10^5 nm^3. By looking at Figure 3, one notices that some pores disappear as the annealing time increases. Pore 7 is not visible after 3 640 s whereas only pores 3 and 6 are still visible after 8 800 s. In the following section, the formation and further dissolution of pores is discussed based on the literature and thanks to original models.

4. Discussion

4.1 Modeling of the formation of pores during annealing of HPT-processed Al-Zr alloy

4.1.1 Excess free volume released by non-equilibrium grain boundaries

Several kinds of solicitation can lead to the formation of pores (cavities) in alloys. Among these solicitations are high temperature deformation and irradiation. In the former case, models have been proposed to predict the kinetics and thermodynamic of pore formation [36,37]. In the later case, pores may be the result of He condensation [38]. Though these solicitations differ from the case studied in the present work, it is relevant to at least consider

the physical model of cavity formation during high temperature deformation in order to later be able to distinguish it from the model we propose. In their paper [37], Raj and Ashby have developed a model to describe the nucleation kinetic of pores along GBs based on the classical nucleation theory. This model was developed to predict the kinetics of intergranular fracture at high temperature. It accounted for a tensile stress acting across a GB, which may result in the formation of pores that may later coalesce and therefore generate a fracture. Both the critical radius of pores and their nucleation barrier were found to depend on the amplitude of this tensile stress. These results were in agreement with the model proposed by Hull and Rimmer [36], who also studied theoretically the growth of GB pores under stress.

The physical model associated to the formation of pores in an alloy previously subjected to SPD is undoubtedly very different. The observed formation of pores in the beginning of annealing and their slow disappearance with further continuation of the heat treatment is more likely associated with a rapid agglomeration of vacancies at multiple GB junctions followed by a release of vacancies in a second stage. Working on a closer topic, Vetrano et al. [39] have shown that pores may form along GBs of Al-Mg-Mn alloys during a quench applied after superplastic deformation. The authors have concluded that pores result from the localized excess vacancies formed during GB sliding. They are also shown that cavities were not stable upon ageing at 175 °C.

In the present work, instead of considering a tensile stress acting on GBs, we have accounted for the structure of defects and their interactions in the GB plane. The GBs in metals and alloys subjected to SPD are often in non-equilibrium state [1,40]. Non-equilibrium GBs (NEQ GBs) in materials either contain less uniformly distributed constituent structural units than in the equilibrium GBs (EQ GBs) with the same misorientation angle, and/or contain additional external dislocations, that leads to an excess free volume and an excess energy of GBs [41–43]. As was demonstrated in [42,44], GBs in commercial purity (CP) Al, processed by HPT with exactly the same regime as used for HPT processing Al-0.4Zr alloy, are mainly NEQ high-angle GBs.

The transition of GBs from a non-equilibrium state to a more equilibrium one should be accompanied by the loss of the excess free volume. Excess vacancies, from which the pores are formed during annealing, can consequently arise in the process of dissolution of the excess free volume contained in NEQ GBs during their relaxation under annealing. It is hence relevant to compare the predicted excess free volume with the dimensions of pores revealed experimentally.

Our experiments did show that the pores are formed mainly at GB junctions (Figure 2) (see also the supplemental information for additional information about the location of pores). We can estimate the summary excess free volume of three NEQ GBs which form a triple junction. According to literature data [45–50], the excess free volume of NEQ GBs is equal to 3-10 % of the equilibrium GB volume. Dilatometric investigation of aluminum alloys (Al-4%Cu-0.5%Zr) processed by HPT at RT was performed in [45,46]. The authors reported that the free volume of NEQ GBs exceeded the free volume of EQ GBs by at least 3 %. It was also concluded that the areas nearby to NEQ GBs were also characterized by increased free volume [50]. An increased width of NEQ GBs compared with the width of EQ GBs was noted in a number of works [50–53]. The increase in GB width is associated with the presence of defects introduced into the GB from the grain body, mainly lattice dislocations, which results in changes of physical properties of GBs, for example, charge scattering at the GB [44,53]. The estimates of the width δ of NEQ GBs based on the measurement of electrical resistance [52,53] and Mössbauer spectra [51] gave the following values: $\delta \approx 2.1$ and 3.7 nm for HPT-processed high purity Cu and Ni, respectively [52], $\delta \approx 9$ nm for HPT-processed CP Al [53] and $\delta \approx 8.4$ nm for UFG Fe [51]. Thus, physical width of NEQ GBs in metals is much larger than their crystallographic width, the latter equaling to 2-3 interatomic distances [50]. According to theoretical investigations, the relative free volume of the NEQ GB in Al is approximately 0.35 (relative to the perfect crystal without GB with the same number of atoms), and the relative excess free volume of the NEQ GB is 0.05–0.10 [49].

One can consequently estimate the total excess free volume of three NEQ GBs which form a triple junction. For a grain size of 1 000 nm and the physical width of NEQ GBs of about 9 nm [50], the excess free volume of the three GBs varies in the limits of (0.9-2.7) 10^6 nm^3.

As shown in Table 2, the typical diameter of pores is d_p ~ 40-60 nm. However, larger pores with d_p ~ 90 nm are also observed. The biggest observed pore of non-spherical shape has the largest dimension which does not exceed 120 nm (pore 1 in Figure 3b). Typical volumes of pores are estimated about 0.5 10^5 nm^3 to 3.5 10^5 nm^3. Thus, the obtained estimates for the observed pore volume and the summary excess free volume of three GBs which form a triple junction are comparable, the latter being even greater (by a factor 10).

One must however keep in mind the fact that the thin foil geometry may alter the kinetics of microstructural evolution with respect to the bulk material. Indeed, the thin foil has a nearly two-dimensional geometry, with a small thickness (< 50 nm) compared the planar

dimension of the specimen. As a consequence, free surfaces, which act as sinks for vacancies, are extremely close compared to a bulk state. The main impact in this study is that a significant fraction of vacancies is expected to annihilate on free surfaces during the in-situ annealing. The experimental hence implies that a significant fraction of excess vacancies may not contribute to the formation of pores. This may explain why the estimated volume of pores observed is an order of magnitude larger than the expected excess free volume of GBs.

The vacancies, formed as a result of such GB compaction, will go to the nearest sinks and form pore by their accumulation. Positive wedge disclinations at triple junctions and GBs [54] are obviously the most effective sinks. During the formation of pores, there is a relaxation of the GBs due to a decrease of the excess free volume of GBs. But, at the same time, not all external (extrinsic) GB dislocations (EGBDs) manage to annihilate. The part of EGBDs, the Burgers vectors of which do not allow to slide along the GBs, can only climb, and climbing is always slow and long process. It hence seems that the formation of pores on disclinations at triple junctions and the climb of EGBDs that form these disclinations should go with significantly different velocities. Pores will grow rapidly on disclinations, which do not have sufficient time to "dissolve" in this short while. Based on these considerations, a model accounting for the major role of disclinations in the formation of pore is presented hereafter.

4.1.2. Model accounting for the role of disclinations in the formation of pores

On one hand, the formation of such pores (cavities) decreases the strain energy of the crystal. However, on the other hand, it increases the crystal energy due to the formation of the pore free surface. The balance of these decrease (which is proportional to d_p^3) and increase (which is proportional to d_p^2) gives an estimate of the equilibrium pore diameter d_p^{eq}. To make such an estimate, one can compare two elastically isotropic cylinders: a solid one and a hollow one, each of which contains a wedge disclination of strength ω on its axis. The strain energy (per unit length of the cylinder) of the solid disclinated cylinder of radius R is [54]:

$$W_s = \frac{D\omega^2 R^2}{8} \tag{1}$$

where $D = G/[2\pi(1-\nu)]$, G is the shear modulus and ν is the Poisson ratio. The total energy W_t of the hollow disclinated cylinder of the same outer radius R and with the inner radius R_0 is the sum of its strain energy W_h which is given by [54]:

$$W_h = \frac{D\omega^2 R^2}{8}\left(1 - t^2 - \frac{4t^2}{1-t^2}(\ln t)^2\right) \tag{2}$$

where $t = R_0/R < 1$, and the surface energy W_γ of the hole, which can be approximated as $W_\gamma \approx 2\pi R_0 \gamma$ with γ being the specific surface energy of the material. In its turn, this γ can be approximated as $\gamma \approx Db^2/2$, where b is the interatomic distance. Then the total energy reads

$$W_t = W_h + W_\gamma \approx \frac{D\omega^2 R^2}{8}\left(1 - t^2 - \frac{4t^2}{1-t^2}(\ln t)^2\right) + \pi DbRt\,. \tag{3}$$

Figure 4 shows the dependence $W_t(t)$ for $G = 27$ GPa, $\nu = 0.31$, $b \approx 0.25$ nm, $R = 250$ nm, and various values of ω. It is seen that at certain values of ω, there are equilibrium values t_{eq} of the ratio $t = R_0/R$, from which the corresponding equilibrium values $R_{0,eq}$ of the internal radius of the cylinder can be obtained. For example, for $\omega = 6°$ we get $R_{0,eq} \approx 45$ nm.

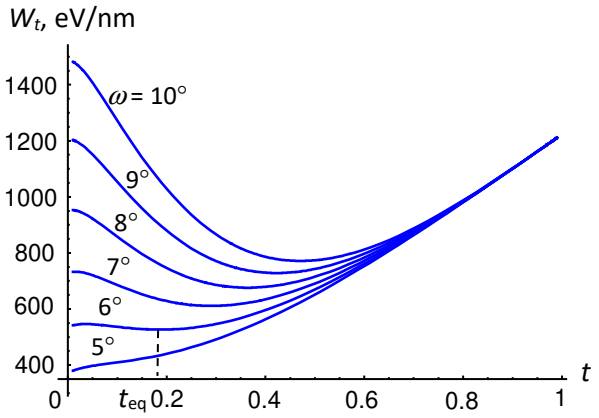

Figure 4 : Dependence $W_t(t)$ for G=27 GPa, ν = 0.31, b ≈0.25 nm, R = 250 nm and various values of ω

Let us now consider the critical conditions which are necessary for the transformation of the solid disclinated cylinder into a hollow one. Such a transformation is accompanied by the corresponding change in the total energy of the cylinder:

$$\Delta W = W_t - W_s = \pi DbRt - \frac{D\omega^2 R^2}{8}\left(t^2 + \frac{4t^2}{1-t^2}(\ln t)^2\right) \tag{4}$$

After some algebra, the energy change takes the form:

$$\Delta W = \frac{DR_0^2}{8}\left\{8\pi\frac{b}{R_0} - \omega^2\left(1 + \frac{4}{1-t^2}(\ln t)^2\right)\right\} \tag{5}$$

The transformation is energetically favorable if $\Delta W < 0$. With Eq. (5), this inequality can be rewritten as follows:

$$\frac{8\pi b}{\omega^2 R} < t + \frac{4t}{1-t^2}(\ln t)^2 \ . \tag{6}$$

Let us denote the right-hand side of this inequality as $f_1(t)$ and its left-hand side as $f_2(\omega)$. The functions $f_1(t)$ (blue curve) and $f_2(\omega)$ (red straight lines) are plotted together in Figure 5 for the aforementioned values of the system parameters. As is seen, in dependence on the disclination strength value, the inequality (6) can either have or not a solution. Indeed, for example, there is no solution for $\omega = 5°$, because in this case $f_1 < f_2$ for any *t*. This means that the disclination strength is not high enough to make the formation of the pore energetically favorable. The same conclusion follows from the behavior of the corresponding curve in Figure 4, which monotonically raises with *t*.

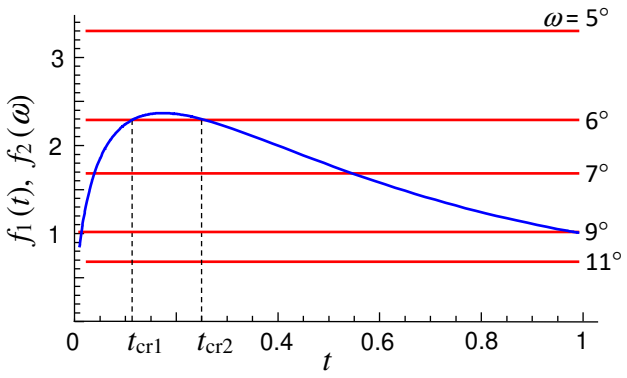

Figure 5 : The functions $f_1(t)$ (blue curve) and $f_2(w)$ (red lines) for G = 27 GPa, ν = 0.31, b ≈ 0.25 nm, R = 250 nm and various values of ω.

In contrast, for $\omega \geq 6°$, the solution exists in the interval $t_{cr1} < t < t_{cr2}$ between the points of intersection of the curve $f_1(t)$ with the lines $f_2(\omega)$ (Figure 5). For example, at

$\omega = 6°$ and $R = 250$ nm, we have $R_{0,cr1} = Rt_{cr1} \approx 28$ nm and $R_{0,cr2} = Rt_{cr2} \approx 63$ nm. With rising ω, this interval rapidly increases and occupies all the range of t, when $t_{cr1} \to 0$ and $t_{cr2} \to 1$ already at $\omega \approx 9°$. For $\omega > 9°$, the transformation of a solid disclinated cylinder into the hollow one is energetically favorable for any *t*.

During the further annealing, the dissolution of the pores and the "disappearance" of the disclinations will go in parallel, stimulating each other. The model describing the concomitant dissolution of pores is introduced in the next section.

4.2 Modeling of the pore dissolution during annealing of HPT-processed Al-Zr alloy

Let us consider a model of consequent dissolution of pores located in triple junctions of GBs during the annealing. It is known that during annealing, NEQ GBs (GBs containing EGBDs) decrease their energy because of a decrease in the number of the EGBDs at these GBs. The process of decreasing the density of the EGBDs at the GBs is usually associated with their emission from GBs and/or moving of the EGBDs to sinks. The pores are the effective sinks for the EGBDs.

In the framework of the model, it is assumed that the driving force of the pore dissolution during annealing is the decrease in the density of the EGBDs as a result of their climb along the GBs towards the pores. The decrease in the number of the EGBDs leads to the decrease in the strain energy of GB disclination configurations characterized by wedge disclinations.

Thus, during the annealing, the dissolution of the triple junction pores and the climb of EGBDs along the GBs goes in parallel, stimulating each other. The decrease of the pore size (pore healing) occurs through the emission of vacancies which migrate mainly along the neighboring GBs due to their enhanced permeability for mass transport. The flux of emitted vacancies provides the climb of EGBDs which therefore effectively increase their mobility along the GBs. As a result, one part of EGBDs of opposite signs annihilates while the remaining part of them climbs towards triple junctions of GBs. Climbing closer to a disclinated triple junction, these EGBDs decrease the strain energy of the wedge disclinations, thus forming a positive feedback, because such a decrease in the strain energy of the disclination structure stimulates further dissolution of the triple junction pores.

Figure 6 shows a two-dimensional model of dissolution of a triple junction pore as a result of the climb of EGBDs along the GBs adjacent to the pore. In the initial state, there is a cylindrical pore of radius r_0, which has formed at a positive wedge triple junction disclination (not shown in Figure 6a and b) of strength $+\omega$ ($+\omega$-disclination) created by three walls of EGBDs, which are shown as walls of climbing edge dislocations with lines parallel to the pore axis and spaced periodically with an average spacing s (Figure 6a). Within the model, a symmetric situation is considered when the GBs adjacent to the pore make the same angles 120° between each other and are characterized by the same linear density $1/s$ of the EGBDs. As the EGBDs climb toward the pore, their number and the pore radius r_n decrease: $r_n < r_0$ (Figure 6b). For the sake of simplicity, the periodicity $s$of the EGBD walls remains however constant within the model. For convenience of further calculations, the walls of EGBDs are modeled by dipoles of the wedge disclinations of strength $\pm\omega/3$ ($\pm\omega/3$ - disclination dipole) (Figure 6c and Figure 6d).

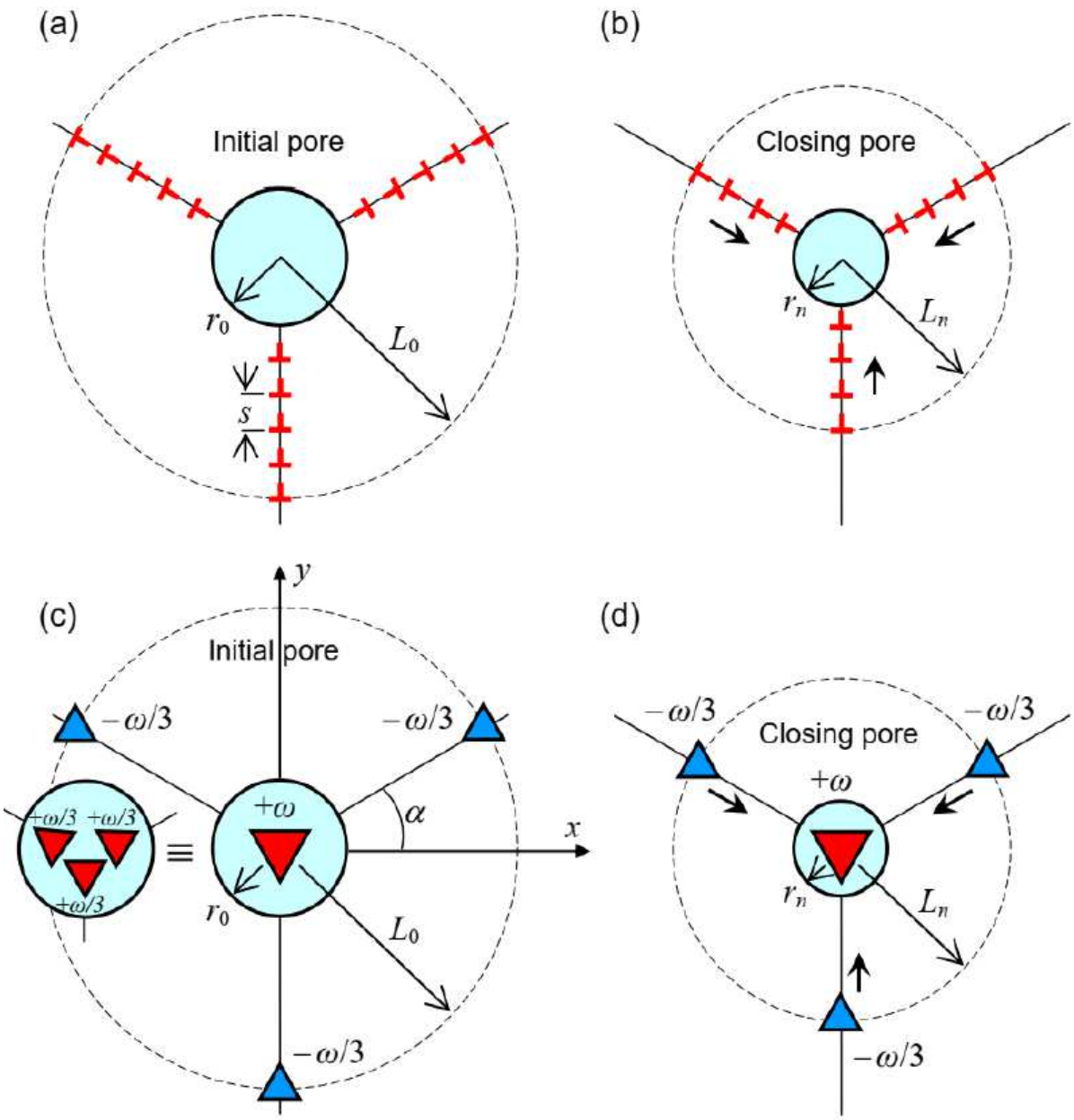

Figure 6: Model of the triple junction pore dissolution due to climb of EGBDs during annealing. (a) The initial configuration of the EGBDs near the pore. (b) Decrease of the pore size due to the climb of the EGBDs towards the pore along the GBs. (c) Modeling the walls of EGBDs by dipoles of wedge disclinations which form a disclination quadrupole. (d) Pore dissolution due to a decrease in the arm of the disclination quadrupole.

The negative $-\omega/3$-disclinations together with the central positive $+\omega$-disclination form a disclination quadrupole with arm L_0, consisting of three disclination dipoles of the same strength $\pm\omega/3$ ($\pm\omega/3$ - disclination quadrupole) (Figure 6c). In this case, the climb of the EGBDs to the pore is equivalent to the decrease in the arm of this quadrupole, which leads to a decrease in its strain energy (Figure 6d).

Let us consider the energy characteristics of the initial stage of the pore dissolution as a result of the decrease in the arm of the $\pm\omega/3$-disclination quadrupole. In this case, the assumption that $L_0 >> r_0$ allows one not to take into account the effect of the pore free surface on the strain energy of the disclination quadrupole. The initial arm L_0 of the quadrupole is assumed to be smaller than the lengths of the GBs adjacent to the triple junction. However it is of the same order of magnitude as the average length of GBs in the area under consideration.

Let us calculate the change in the strain energy, which corresponds to the decrease of the arm of the disclination quadrupole by a distance $p_n = ns$ (where n is the number of the EGBDs absorbed by the pore from each GB), accompanied by the decrease in the pore radius $r_n = r_0 - 3p_n/2\pi$. In doing so, we study the defect system transformation from the $(n-1)$-th state with a total energy W_{n-1}, corresponding to the disclination quadrupole with the arm $L_{n-1} = L_0 - p_{n-1}$, to the n-th state with a total energy W_n, corresponding to the disclination quadrupole with the arm $L_n = L_0 - p_n$. Such a transformation of the defect system is energetically favorable if $\Delta W_n = W_n - W_{n-1} < 0$.

The energy difference ΔW_n (per unit length of the pore) is determined by the expression:

$$\Delta W_n = 3E_{s(n)} + 3E_{i(n)} + E_{\gamma(n)} + 3E_{GB(n)} - 3E_{s(n-1)} - 3E_{i(n-1)} - E_{\gamma(n-1)} - 3E_{GB(n-1)}, \qquad (7)$$

where $E_{s(n-1)}$ and $E_{s(n)}$ are the self strain energies of the $\pm\omega/3$-disclination dipole in the $(n-1)$-th and n-th states of the defect system, respectively; $E_{i(n-1)}$ and $E_{i(n)}$ are the energies of elastic interaction between two $\pm\omega/3$-disclination dipoles in the $(n-1)$-th and n-th states of the defect system, respectively; $E_{\gamma(n-1)}$ and $E_{\gamma(n)}$ are the surface energy of the pores in the $(n-1)$-th and n-th states of the defect system, respectively; $E_{GB(n-1)}$ и $E_{GB(n)}$ are the energies specifying GB segments which appear after the pore dissolution in the $(n-1)$-th and n-th states of the defect system, respectively.

The self energy $E_{s(n)}$ of the $\pm\omega/3$ -disclination dipole is given by standard formula [54]:

$$E_{s(n)} = \frac{D\theta^2 L_n^2}{2}\left(\ln\frac{R}{L_n} + \frac{1}{2}\right), \tag{8}$$

where $\theta = \omega/3$ and $R \approx 2L_0$ is the cut-off radius of the stress fields of $\pm\omega/3$ -disclination dipole.

To calculate the interaction energy $E_{i(n)}$ between two disclination dipoles, we used the standard procedure of calculating the work spent to nucleate one defect in the stress field of another defect. It is given by the following expression:

$$\begin{aligned} E_{i(n)} = \frac{D\theta^2}{4}\Bigg(& R^2 \ln\frac{R^2}{R^2 + L_n^2} + L_n^2 \ln\left[1 + \frac{L_n[L_n(1+2\cos\alpha) - 2R\sin\alpha]}{R^2 + L_n^2}\right] + \\ & + [L_n^2(1+2\cos\alpha) - R(R + 2L_n\sin\alpha)]\ln\left[1 + \frac{L_n^2(1+2\cos\alpha)}{R^2 - 2RL_n\sin\alpha + L_n^2}\right]\Bigg). \end{aligned} \tag{9}$$

The energies $E_{s(n-1)}$ and $E_{i(n-1)}$ are obtained from Eqs. (8) and (9), respectively, by a simple replacement of L_n by L_{n-1}.

The energies $E_{\gamma(n-1)}$ and $E_{\gamma(n)}$ are given by standard formulas, respectively:

$$E_{\gamma(n-1)} = 2\pi r_{(n-1)}\gamma_s, \tag{10}$$

$$E_{\gamma(n)} = 2\pi r_n \gamma_s, \tag{11}$$

where γ_s is the specific surface energy of the pore.

The energies $E_{GB(n-1)}$ and $E_{GB(n)}$ are

$$E_{GB(n-1)} = p_{(n-1)}\gamma_{GB}, \tag{12}$$

$$E_{GB(n)} = p_{(n)}\gamma_{GB}, \tag{13}$$

where γ_{GB} is the specific energy of the GB (for simplicity, we assume that γ_{GB} is the same for all the three GBs adjacent to the pore).

Using Eqs. (7) to (13), we calculated the energy difference ΔW_n in dependence on the p_n distance for various values of the quadrupole arm L_0 in the exemplary cases of UFG Al-Zr alloy. Doing this, the following values of parameters have been exploited: G = 27 GPa,

$\nu = 0.31$, $\gamma_s = 1.5$ J m^{-2}, $\gamma_{GB} = 0.5$ J m^{-2}, and $b_{gb} \approx 0.1$ nm. Other parameters of the defect system were taken as $\omega \approx b_{gb}/s$, $s = 0.5$ nm, $r_0 = 100$ nm, and $\alpha = 30°$.

Figure 7 shows the predicted variations of $\Delta W_n(p_n)$ for the case of UFG Al-Zr alloy at various quadrupole arms L_0. It can be seen that the process of the disclination quadrupole arm decreasing is energetically favorable ($\Delta W_n < 0$) for the chosen parameters of the defect structure. Thus, it is demonstrated that the process of the pore dissolution can be realized due to the successive climb of EGBDs along the GBs to the pore.

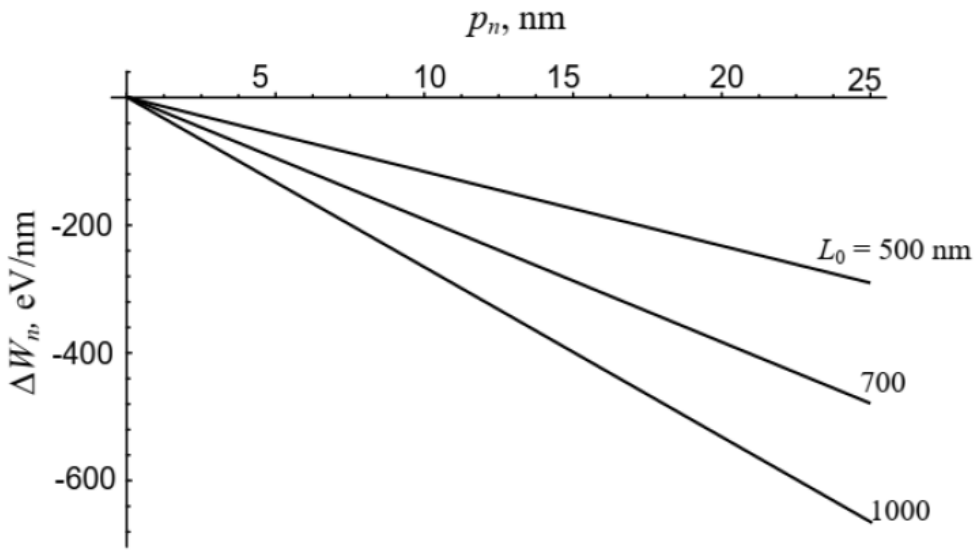

Figure 7: Dependence of the energy change ΔW_n on the distance p_n for various values of the quadrupole arm $L_0 \approx 500$, 700 and 1000 nm.

With decreasing the pore size, more vacancies are released, which assist the climb of EGBDs and, therefore, the quadrupole arm correspondingly decreases. As a result, the strain energy of the disclination quadrupole decreases too. This stimulates further dissolution of the pore. Thus, a positive feedback applies. Along with this process, the precipitation and growth of precipitates can occur, possibly at the GB disclinations of the opposite sign. By "cleaning" GBs from EGBDs during longer annealing, triple junction disclinations and pores reduce the role of GBs as sources of lattice dislocations under external loading, hence the hardening after annealing will take place. This is in agreement with the model proposed earlier to explain the hardening by annealing in HPT-processed CP Al [55,56].

5. Conclusion

In-situ annealing in STEM offers the possibility to reveal phenomena which are hardly accessible by conventional experimental protocols and post-processing observations. An original experiment was designed here to elucidate the mechanisms at stake during the early stages of annealing of a model aluminium alloy (Al-0.4wt%Zr) previously subjected to SPD. Our study demonstrates that the rapid rearrangement of NEQ GBs provokes the liberation of a significant excess free volume, initially stored in the NEQ GBs, which results in the quasi immediate formation of pores (already observed after 75 s at 230 °C). This fast process is explained by the migration of vacancies to GB triple junctions. Though this change in the GB structure does not involve any GB migration, local change in the configuration of some GBs could be observed. Straightening of some of them, approaching the angles between them to 120 degrees was observed.

The typical pore size was 40-80 nm and the volume of pores is in perfect agreement with the values of excess free volume calculated. As annealing proceeds, the experiment reveals the subsequent slow resorption of these pores with the complete disappearance of some of them, which indicates a release of vacancies in a second stage.

To explain the aforementioned experimental observations, original theoretical models have been introduced. The first model describes the pore formation at disclinated triple junctions as a thermodynamically driven process of free volume dissolution through generation of vacancies which then migrate to the triple junctions and coagulate at them with growth of the pores diminishing the strain energy of the triple junction disclinations. Within the model, we have calculated the equilibrium pore radius $R_{0,eq}$ and the critical pore radii $R_{0,cr1}$ and $R_{0,cr2}$, in the range of which the pore existence is energetically favorable at a triple junction disclination. We have shown that both the equilibrium pore radius $R_{0,eq}$ and critical interval $[R_{0,cr1}, R_{0,cr2}]$ increase with the strength of the triple junction disclination. We have also demonstrated that the free volume stored in the NEQ GBs, adjacent to a triple junction, is large enough for creation of an observable pore at the triple junction during fast transformation of the NEQ GBs into more equilibrium GBs under fast annealing.

The second model describes a further decrease of the triple junction disclination strain energy through the climb of EGBDs towards the hollow disclinated triple junctions,

accompanied with dissolution of the triple junction pores by emission of vacancies which assist the dislocation climb in the course of long-term annealing. In the framework of the model, we have calculated the energy difference ΔW_n, caused by the shrinkage of the disclination structure around a hollow disclinated triple junction, and shown that this shrinkage is energetically favorable. Thus, we have proved that the process of the pore dissolution can be realized due to the successive climb of EGBDs along the GBs to the triple junction pore.

The revealed features of the GB structure evolution during low-temperature annealing of UFG Al-Zr alloys opens a new GB engineering approach to increase the strength of these materials at elevated temperatures. Moreover, this work will help understanding the accelerated precipitation kinetics observed in similar system, by accounting for the behavior and amount of vacancies available for low temperature annealing of such alloy systems.

Acknowledgments

In situ STEM experiments have been performed on the GENESIS platform supported by the Région Normandie, the Métropole Rouen Normandie, the CNRS via LABEX EMC3 and the French National Research Agency as a part of the program "Investissements d'avenir" with the reference ANR-11-EQPX-0020. N.V.S. and M.Yu.G. are thankful to the Institute for Problems in Mechanical Engineering of the Russian Academy of Sciences, and T.S.O. is thankful to the Ioffe Institute of the Russian Academy of Sciences for their support (within the corresponding state tasks) in development of the theoretical models figuring in the paper.

References

[1] R.Z. Valiev, R.K. Islamgaliev, I. V. Alexandrov, Bulk nanostructured materials from severe plastic deformation, Prog. Mater. Sci. 45 (2000) 103–189. https://doi.org/10.1016/S0079-6425(99)00007-9.

[2] R.Z. Valiev, I. V. Alexandrov, Y.T. Zhu, T.C. Lowe, Paradox of strength and ductility in metals processed by severe plastic deformation, J. Mater. Res. 17 (2002) 5–8. https://doi.org/10.1557/JMR.2002.0002.

[3] X. Sauvage, G. Wilde, S. V. Divinski, Z. Horita, R.Z. Valiev, Grain boundaries in ultrafine grained materials processed by severe plastic deformation and related phenomena, Mater. Sci. Eng. A. 540 (2012) 1–12. https://doi.org/10.1016/j.msea.2012.01.080.

[4] Y.H. Zhao, X.Z. Liao, Z. Jin, R.Z. Valiev, Y.T. Zhu, Microstructures and mechanical properties of ultrafine grained 7075 Al alloy processed by ECAP and their evolutions during annealing, Acta Mater. 52 (2004) 4589–4599. https://doi.org/10.1016/j.actamat.2004.06.017.

[5] A. Deschamps, G. Fribourg, Y. Bréchet, J.L. Chemin, C.R. Hutchinson, In-situ evaluation of dynamic precipitation during plastic straining of an Al-Zn-Mg-Cu alloy, Acta Mater. 60 (2012) 1905–1916. https://doi.org/10.1016/j.actamat.2012.01.002.

[6] G. Sha, Y.B. Wang, X.Z. Liao, Z.C. Duan, S.P. Ringer, T.G. Langdon, Influence of equal-channel angular pressing on precipitation in an Al-Zn-Mg-Cu alloy, Acta Mater. 57 (2009) 3123–3132. https://doi.org/10.1016/j.actamat.2009.03.017.

[7] S.S. Wang, J.T. Jiang, G.H. Fan, A.M. Panindre, G.S. Frankel, L. Zhen, Accelerated precipitation and growth of phases in an Al-Zn-Mg-Cu alloy processed by surface abrasion, Acta Mater. 131 (2017) 233–245. https://doi.org/10.1016/j.actamat.2017.03.074.

[8] X. Sauvage, A. Duchaussoy, G. Zaher, Strain Induced Segregations in Severely Deformed Materials, Mater. Trans. 60 (2019) 1151-1158. https://doi.org/10.2320/matertrans.MF201919.

[9] I. Semenova, G. Salimgareeva, G. Da Costa, W. Lefebvre, R. Valiev, Enhanced strength and ductility of ultrafine-grained Ti processed by severe plastic deformation, Adv. Eng. Mater. 12 (2010) 803-807. https://doi.org/10.1002/adem.201000059.

[10] P. V. Liddicoat, X.Z. Liao, Y. Zhao, Y. Zhu, M.Y. Murashkin, E.J. Lavernia, R.Z. Valiev, S.P. Ringer, Nanostructural hierarchy increases the strength of aluminium alloys, Nat. Commun. 1 (2010) 1–7. https://doi.org/10.1038/ncomms1062.

[11] S.M. Reddy, N.E. Timms, P. Trimby, P.D. Kinny, C. Buchan, K. Blake, Crystal-plastic deformation of zircon: A defect in the assumption of chemical robustness, Geology. 34 (2006) 257–260. https://doi.org/10.1130/G22110.1.

[12] X. Sauvage, A. Ganeev, Y. Ivanisenko, N. Enikeev, M. Murashkin, R. Valiev, Grain Boundary Segregation in UFG Alloys Processed by Severe Plastic Deformation, Adv. Eng. Mater. 14 (2012) 968–974. https://doi.org/10.1002/adem.201200060.

[13] G. Saada, Les défauts ponctuels produits par écrouissage dans les métaux, J. Phys. 24 (1963) 426–430. https://doi.org/10.1051/jphys:01963002407042600.

[14] A.L. Ruoff, R.W. Balluffi, On strain-enhanced diffusion in metals. III. Interpretation of recent experiments, J. Appl. Phys. 34 (1963) 2862–2872. https://doi.org/10.1063/1.1729822.

[15] R. Würschum, W. Greiner, R.Z. Valiev, M. Rapp, W. Sigle, O. Schneeweiss, H.E. Schaefer, Interfacial free volumes in ultra-fine grained metals prepared by severe plastic deformation, by spark erosion, or by crystallization of amorphous alloys, Scr. Metall. Mater. 25 (1991) 2451–2456. https://doi.org/10.1016/0956-716X(91)90048-6.

[16] S. Van Petegem, F. Dalla Torre, D. Segers, H. Van Swygenhoven, Free volume in nanostructured Ni, Scr. Mater. 48 (2003) 17–22. https://doi.org/10.1016/S1359-6462(02)00322-6.

[17] H. Mecking, Y. Estrin, The effect of vacancy generation on plastic deformation, Scr. Metall. 14 (1980) 815–819. https://doi.org/10.1016/0036-9748(80)90295-1.

[18] D. Setman, E. Schafler, E. Korznikova, M.J. Zehetbauer, The presence and nature of vacancy

type defects in nanometals detained by severe plastic deformation, Mater. Sci. Eng. A. 493 (2008) 116–122. https://doi.org/10.1016/j.msea.2007.06.093.

[19] Y. Huang, J.D. Robson, P.B. Prangnell, The formation of nanograin structures and accelerated room-temperature theta precipitation in a severely deformed Al-4 wt.% Cu alloy, Acta Mater. 58 (2010) 1643–1657. https://doi.org/10.1016/j.actamat.2009.11.008.

[20] W. Lechner, W. Puff, B. Mingler, M.J. Zehetbauer, R. Würschum, Microstructure and vacancy-type defects in high-pressure torsion deformed Al-Cu-Mg-Mn alloy, Scr. Mater. 61 (2009) 383–386. https://doi.org/10.1016/j.scriptamat.2009.04.027.

[21] A. V. Kazantzis, Z.G. Chen, J.T.M. De Hosson, Deformation mechanism of aluminum-magnesium alloys at elevated temperatures, J. Mater. Sci. 48 (2013) 7399–7408. https://doi.org/10.1007/s10853-013-7555-7.

[22] K.E. Knipling, D.C. Dunand, D.N. Seidman, Precipitation evolution in Al-Zr and Al-Zr-Ti alloys during aging at 450-600 ??C, Acta Mater. 56 (2008) 1182–1195. https://doi.org/10.1016/j.actamat.2007.11.011.

[23] K.E. Knipling, D.C. Dunand, D.N. Seidman, Precipitation evolution in AlZr and Al Zr Ti alloys during isothermal aging at 375 - 425 °C, Acta Mater. 56 (2008) 114–127. https://doi.org/10.1016/j.actamat.2007.09.004.

[24] K.E. Knipling, D.C. Dunand, D.N. Seidman, Criteria for Developing Castable, Creep-Resistant Aluminum-Based Alloys A Review, Zeitschrift F{ü}r Met. 97 (2006) 246–265.

[25] K.E. Knipling, D.C. Dunand, D.N. Seidman, Nucleation and Precipitation Strengthening in Dilute Al-Ti and Al-Zr Alloys, Metall. Mater. Trans. A. 38 (2007) 2552–2563. https://doi.org/10.1007/s11661-007-9283-6.

[26] W. Lefebvre, N. Masquelier, J. Houard, R. Patte, H. Zapolsky, Tracking the path of dislocations across ordered Al_3Zr nano-precipitates in three dimensions, Scripta Mater. 70 (2014) 43-46. https://doi.org/10.1016/j.scriptamat.2013.09.014.

[27] N. Masquelier, Caractérisation et modélisation de transformations microstructurales pour la mise au point d'une nouvelle génération d'alliages d'aluminium pour conducteurs électriques, PhD Thesis, Université de Rouen (2012) Http://Www.Theses.Fr. (2012). http://www.theses.fr/2012ROUES011 (accessed June 24, 2020).

[28] T.S. Orlova, A.M. Mavlyutov, T.A. Latynina, E. V Ubyivovk, M.Y. Murashkin, R. Schneider, D. Gerthsen, R.Z. Valiev, Influence of severe plastic deformation on microstructure, strength and electrical conductivity of aged Al–0.4 Zr (wt.%) alloy, Reviews on Advanced Materials Science (2018) 55(1) 92-101. https://doi.org/10.1515/rams-2018-0032.

[29] T.S. Orlova, T.A. Latynina, A.M. Mavlyutov, M.Y. Murashkin, R.Z. Valiev, Effect of annealing on microstructure, strength and electrical conductivity of the pre-aged and HPT-processed Al-0.4Zr alloy, J. Alloys Compd. 784 (2019) 41–48. https://doi.org/10.1016/j.jallcom.2018.12.324.

[30] T.A. Latynina, A.M. Mavlyutov, M.Y. Murashkin, R.Z. Valiev, T.S. Orlova, The effect of hardening by annealing in ultrafine-grained Al–0.4Zr alloy: influence of Zr microadditives, Philos. Mag. 99 (2019) 2424–2443. https://doi.org/10.1080/14786435.2019.1631501.

[31] R.Z. Valiev, I. V. Alexandrov, Nanostructured materials from severe plastic deformation, Nanostructured Mater. 12 (1999) 35–40. https://doi.org/10.1016/S0965-9773(99)00061-6.

[32] A.P. Zhilyaev, T.G. Langdon, Using high-pressure torsion for metal processing: Fundamentals and applications, Prog. Mater. Sci. 53 (2008) 893–979. https://doi.org/10.1016/j.pmatsci.2008.03.002.

[33] N.A. Belov, A.N. Alabin, I.A. Matveeva, D.G. Eskin, Effect of Zr additions and annealing temperature on electrical conductivity and hardness of hot rolled Al sheets, Trans. Nonferrous Met. Soc. China (English Ed. 25 (2015) 2817–2826. https://doi.org/10.1016/S1003-6326(15)63907-3.

[34] D.S.Pa. and T.O. R.J. Schoernern U.S. Patent No.3 670 401. Washington, No Title, 1972.

[35] D.E. Jesson, S.J. Pennycook, Incoherent imaging of crystals using thermally scattered electrons, Proc. R. Soc. London. Ser. A Math. Phys. Sci. 449 (1995) 273–293. https://doi.org/10.1098/rspa.1995.0044.

[36] D. Hull, D.E. Rimmer, The growth of grain-boundary voids under stress, Philos. Mag. 4 (1959) 673–687. https://doi.org/10.1080/14786435908243264.

[37] R. Raj, M.F. Ashby, Intergranular fracture at elevated temperature, Acta Metall. 23 (1975) 653–666. https://doi.org/10.1016/0001-6160(75)90047-4.

[38] E.H. Lee, A.F. Rowcliffe, L.K. Mansur, Precipitation and cavity formation in austenitic stainless steels during irradiation, J. Nucl. Mater. 104 (1981) 1475–1480. https://doi.org/10.1016/0022-3115(82)90808-X.

[39] J.S. Vetrano, E.P. Simonen, S.M. Bruemmer, Evidence for excess vacancies at sliding grain boundaries during superplastic deformation, Acta Mater. 47 (1999) 4125–4129. https://doi.org/10.1016/S1359-6454(99)00271-2.

[40] S. V. Divinski, G. Reglitz, H. Rösner, Y. Estrin, G. Wilde, Ultra-fast diffusion channels in pure Ni severely deformed by equal-channel angular pressing, Acta Mater. 59 (2011) 1974–1985. https://doi.org/10.1016/j.actamat.2010.11.063.

[41] A.A. Nazarov, A.E. Romanov, R.Z. Valiev, On the structure, stress fields and energy of nonequilibrium grain boundaries, Acta Metall. Mater. 41 (1993) 1033–1040. https://doi.org/10.1016/0956-7151(93)90152-I.

[42] T.S. Orlova, A. V. Ankudinov, A.M. Mavlyutov, N.N. Resnina, Effect of grain boundaries on the electron work function of ultrafine grained aluminum, Rev. Adv. Mater. Sci. 57 (2018) 110–115. https://doi.org/10.1515/rams-2018-0053.

[43] A.E. Romanov, A.L. Kolesnikova, T.S. Orlova, I. Hussainova, V.E. Bougrov, R.Z. Valiev, Non-equilibrium grain boundaries with excess energy in graphene, Carbon N. Y. 81 (2015) 223–231. https://doi.org/10.1016/j.carbon.2014.09.053.

[44] T.S. Orlova, A.M. Mavlyutov, A.S. Bondarenko, I.A. Kasatkin, M.Y. Murashkin, R.Z. Valiev, Influence of grain boundary state on electrical resistivity of ultrafine grained aluminium, Philos. Mag. 96 (2016) 2429–2444. https://doi.org/10.1080/14786435.2016.1204022.

[45] R.S. Musalimov, R.Z. Valiev, Dilatometric analysis of aluminium alloy with submicrometre grained structure, Scr. Metall. Mater. 27 (1992) 1685–1690. https://doi.org/10.1016/0956-716X(92)90002-V.

[46] R.S. MUSALIMOV, R.Z. VALIEV, Dilatometric study of an aluminum alloy with submicron-grained structure, Phys. Met. Metallogr. 74 (1992) 263-266.

[47] V.N. Chuvil'deev, Non-equilibrium grain boundary in metals, Theory and applications, Fizmatlit, Moscow. (2004).

[48] V.N. Chuvil'deev, Micromechanisms of deformation-stimulated grain boundary self-diffusion. Communication 1. Influence of excess free volume on free energy and diffusion parameters of grain boundaries, Fiz. Met. i Metalloved. 81 (1996) 6–13.

[49] V.N. Chuvil'deev, V.I. Kopylov, W. Zeiger, A theory of non-equilibrium grain boundaries and its applications to nano- and micro-crystalline materials processed by ECAP, in: Ann. Chim. Sci. Des Mater., No longer published by Elsevier, 2002: pp. 55–64. https://doi.org/10.1016/S0151-9107(02)80007-1.

[50] R.Z. Valiev, A.P. Zhilyaev, T.G. Langdon, Bulk Nanostructured Materials, John Wiley & Sons, Inc, Hoboken, NJ, 2013. https://doi.org/10.1002/9781118742679.

[51] R.Z. Valiev, R.R. Mulyukov, V. V. Ovchinnikov, Direction of a grain-boundary phase in submicrometre-grained iron, Philos. Mag. Lett. 62 (1990) 253–256. https://doi.org/10.1080/09500839008215131.

[52] R.K. Islamgaliev, K. Pekala, M. Pekala, R.Z. Valiev, The Determination of the Grain Boundary Width of Ultrafine Grained Copper and Nickel from Electrical Resistivity Measurements, Phys. Status Solidi. 162 (1997) 559–566. https://doi.org/10.1002/1521-396X(199708)162:2<559::AID-PSSA559>3.0.CO;2-Z.

[53] A.M. Mavlyutov, A.S. Bondarenko, M.Y. Murashkin, E. V. Boltynjuk, R.Z. Valiev, T.S. Orlova, Effect of annealing on microhardness and electrical resistivity of nanostructured SPD aluminium, J. Alloys Compd. 698 (2017) 539–546. https://doi.org/10.1016/j.jallcom.2016.12.240.

[54] A.E. Romanov, V.I. Vladimirov, Disclinations in crystalline solids, in: F.R.N Nabarro Dislocations Solids, North-Holland, Amsterdam, Vol. 9, 1992: pp. 191–402.

[55] T.S. Orlova, N. V. Skiba, A.M. Mavlyutov, M.Y. Murashkin, R.Z. Valiev, M.Y. Gutkin, Hardening by annealing and implementation of high ductility of ultra-fine grained aluminum: Experiment and theory, Rev. Adv. Mater. Sci. 57 (2018) 224–240. https://doi.org/10.1515/rams-2018-0068.

[56] M.Y. Gutkin, T.A. Latynina, T.S. Orlova, N. V. Skiba, Mechanism of Hardening of Ultrafine-Grained Aluminum after Annealing, Phys. Solid State. 61 (2019) 1790–1799. https://doi.org/10.1134/S1063783419100160.

Al-0.4wt%Zr alloy processed by severe plastic deformation

In situ annealing at 230°C in STEM

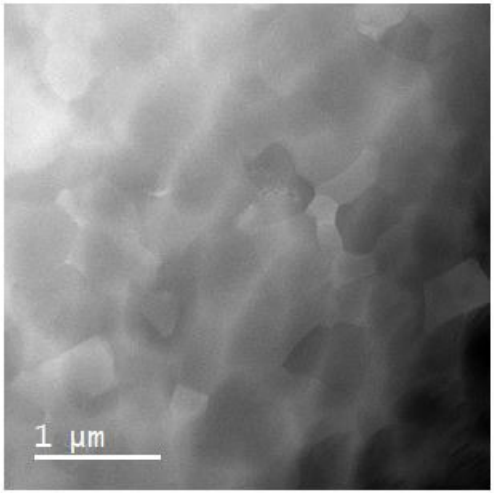

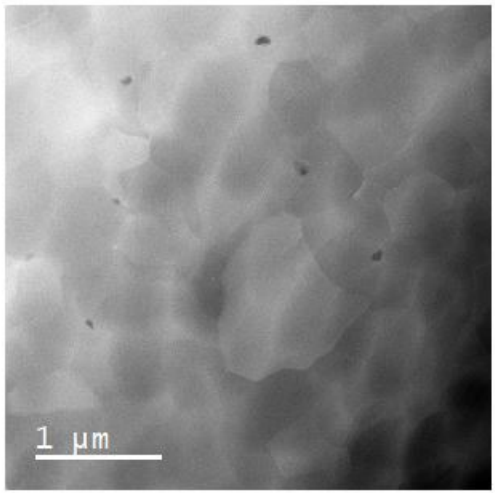

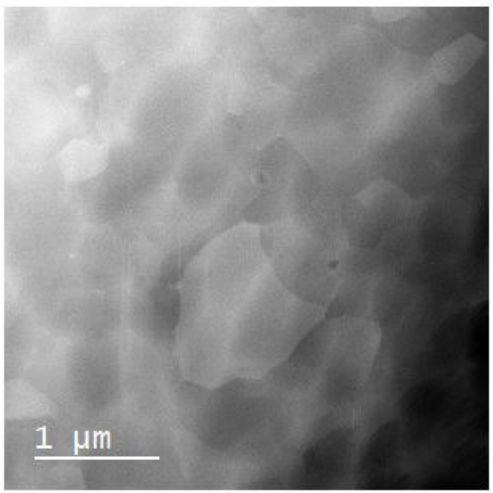

Formation of pores by vacancy release along non equilibrium grain boundaries

Slow resorption of pores by climb of extrinsic grain boundary dislocations